The Astronomical Journal, 168:144 (11pp), 2024 October https://doi.org/10.3847/1538-3881/ad4ecf

κ Andromedae b Is a Fast Rotator from KPIC High-resolution Spectroscopy

Evan C. Morris[1], Jason J. Wang (王劲飞)[2], Chih-Chun Hsu[2], Jean-Baptiste Ruffio[3], Jerry W. Xuan[4], Jacques-Robert Delorme[4,5], Callie Hood[1], Marta L. Bryan[6], Emily C. Martin[1], Jacklyn Pezzato[4], Dimitri Mawet[4,7], Andrew Skemer[1], Ashley Baker[4], Randall Bartos[7], Benjamin Calvin[8], Sylvain Cetre[5], Greg Doppmann[5], Daniel Echeverri[4], Luke Finnerty[8], Michael P. Fitzgerald[8], Nemanja Jovanovic[4], Joshua Liberman[9], Ronald Lopez[8], Ben Sappey[3], Tobias Schofield[4], J. Kent Wallace[7], and Ji Wang (王吉)[10]
[1] Department of Astronomy & Astrophysics, University of California, Santa Cruz, CA 95064, USA; ecmorris@ucsc.edu
[2] Center for Interdisciplinary Exploration and Research in Astrophysics (CIERA), Northwestern University, 1800 Sherman, Evanston, IL 9 60201, USA
[3] Center for Astrophysics and Space Sciences, University of California, San Diego, La Jolla, CA 92093, USA
[4] Department of Astronomy, California Institute of Technology, Pasadena, CA 91125, USA
[5] W. M. Keck Observatory, 65-1120 Mamalahoa Highway, Kamuela, HI, USA
[6] David A. Dunlap Institute Department of Astronomy & Astrophysics, University of Toronto, 50 St. George Street, Toronto, ON M5S 3H4, Canada
[7] Jet Propulsion Laboratory, California Institute of Technology, 4800 Oak Grove Drive, Pasadena, CA 91109, USA
[8] Department of Physics & Astronomy, 430 Portola Plaza, University of California, Los Angeles, CA 90095, USA
[9] James C. Wyant College of Optical Sciences, University of Arizona, Meinel Building 1630 E. University Boulevard, Tucson, AZ 85721, USA
[10] Department of Astronomy, The Ohio State University, 100 W 18th Avenue, Columbus, OH 43210, USA
Received 2024 February 12; revised 2024 May 1; accepted 2024 May 20; published 2024 September 4

Abstract

We used the Keck Planet Imager and Characterizer to obtain high-resolution ($R \sim 35{,}000$) K-band spectra of κ Andromedae b, a planetary-mass companion orbiting the B9V star, κ Andromedae A. We characterized its spin, radial velocity, and bulk atmospheric parameters through use of a forward-modeling framework to jointly fit planetary spectra and residual starlight speckles, obtaining likelihood-based posterior probabilities. We also detected H_2O and CO in its atmosphere via cross correlation. We measured a $v \sin(i)$ value for κ Andromedae b of 38.42 ± 0.05 km s^{-1}, allowing us to extend our understanding of the population of close-in bound companions at higher rotation rates. This rotation rate is one of the highest spins relative to breakup velocity measured to date, at close to 50% of breakup velocity. We identify a radial velocity $-17.35^{+0.05}_{-0.09}$ km s^{-1}, which we use with existing astrometry and radial velocity measurements to update the orbital fit. We also measure an effective temperature of 1700 ± 100 K and a $\log(g)$ of 4.7 ± 0.5 cgs dex.

Unified Astronomy Thesaurus concepts: Exoplanet atmospheres (487); Exoplanet formation (492); High angular resolution (2167); High resolution spectroscopy (2096)

1. Introduction

New capabilities in high-resolution ($R > 10{,}000$) spectroscopy open avenues for further exploration of the orbital and atmospheric parameters of directly imaged planetary-mass companions. In particular, this resolving power allows us to look at the shapes and shifts of individual absorption lines in the planetary and substellar atmospheres to understand properties such as rotation and radial velocity (e.g., Snellen et al. 2014; Ruffio et al. 2019; Bryan et al. 2020; Wang et al. 2021). Further, forward modeling and cross correlation between data and models give us insight into temperatures and compositions (e.g., Konopacky et al. 2013; Brogi & Line 2019; Wang et al. 2022; Xuan et al. 2022; Landman et al. 2024).

Previously, these investigations have been primarily limited to brighter companions located at greater distances from their stars as the instrumentation used for this purpose utilized slit spectroscopy. In these cases, at small angular separation, stellar light would contaminate the data to the point of overwhelming the planetary signal. This problem can be mitigated using Keck Planet Imager and Characterizer (KPIC; Mawet et al. 2017; Jovanovic et al. 2019; Delorme et al. 2021), which is designed to combine single-mode fiber, high-resolution spectroscopy with high-contrast imaging techniques, the combination of which has been shown to significantly decrease the stellar glare present in the data and improve postprocessing possibilities (Wang et al. 2021). This combination of technologies allows for observation of fainter planets at smaller angular separation from their stars.

To date, KPIC has been used to expand NIRSPEC's high-resolution spectroscopy to companions that are smaller separation (typically at or within $\sim 1''$), particularly looking at the spin parameter, radial velocity, and atmospheric information, including molecular detections, abundances, and effective temperature, for the HR 8799 planets (Wang et al. 2021, 2023), HR 7672 B (Wang et al. 2022), HD 4747 B (Xuan et al. 2022), HIP 55507 B (Xuan et al. 2024), and HD 33632 Ab (Hsu 2024).

Understanding planetary spin allows us insight into the system's formation history and evolution. Planetary-mass objects spin up and conserve angular momentum after disk dispersal (Bryan et al. 2020). Recent work shows that companions spin at 10% of breakup velocity generally, and this can be explained by magnetic breaking in the early phases, in the release of angular momentum caused by interaction with the magnetized circumplanetary disk (Batygin 2018; Bryan et al. 2020). There is related tentative evidence of an anticorrelation between spin and companion mass, pending access to a larger sample size of low-mass companion spin measurements (Batygin 2018; Wang et al. 2021; Hsu 2024).

We focus our analysis on κ Andromedae b (hereafter κ And b; Carson et al. 2013). This planetary-mass companion orbits a B9V star, understood to be a potential member of the Columba association, with an age of ~30 Myr (Zuckerman et al. 2011), leading to a mass estimate of $\sim 12.8\,M_{\rm Jup}$ in Carson et al. (2013). However, Hinkley et al. (2013) found a much older isochronal age for this object, 220 ± 100 Myr, corresponding to a mass of $50^{+16}_{-13}\,M_{\rm Jup}$. Following this, Jones et al. (2016) used CHARA interferometry to constrain properties of κ Andromedae A (hereafter κ And A) to compare to evolutionary models, finding that the models favored a younger age of 47^{+27}_{-40} Myr, which is in agreement with the most recent Columba association age estimate of 42^{+6}_{-4} Myr from Bell et al. (2015).

Other studies of κ And b indicate that the object is low gravity (with a $\log(g)$ of 4–4.5 cgs dex), in agreement with models suggesting a lower age (Currie et al. 2018; Uyama et al. 2020). Uyama et al. (2020) and Currie et al. (2018) find a temperature range of 1700–2000 K; Wilcomb et al. (2020) find a range of 1950–2150 K. This appears to be dependent on selected model grid, and the range in Uyama et al. (2020) is found when comparing 13 grids, including the one we chose for this paper. Wilcomb et al. (2020) derives a C/O ratio of $0.70^{+0.09}_{-.24}$ for κ And b, which, when paired with their subsolar metallicity measurement, suggests consistency with the host star and rapid formation via gravitational instability. Currie et al. (2018) estimate a mass of $13^{+13}_{-2}\,M_{\rm Jup}$, which we use in further analysis.[11]

Section 2 describes the observation sequence of κ And b performed with KPIC. Section 3 details the data-reduction process developed for this data set and used broadly for KPIC observations. In Section 4, we describe our forward-modeling framework for fitting atmospheric models to the data, as well as discuss our cross-correlation molecular detections of H_2O and CO in the planet's atmosphere. Section 5 contextualizes our measurements, including the first spin for this object, a new orbital fit based on additional radial velocity data, and analysis of bulk atmospheric parameters. We finish in Section 6 by summarizing our work and discussing future avenues of improvement.

2. Observations

2.1. Instrument Description

The KPIC is an instrument optimized for obtaining high-resolution spectra of directly imaged exoplanets. KPIC includes upgrades to the Keck II adaptive optics (AO) system, paired with a fiber injection unit (FIU) to Keck's existing high-resolution near-infrared spectrograph, NIRSPEC (R~35,000; McLean et al. 1998; Martin et al. 2018). Light is coupled into an array of single-mode fibers, which are fed into the NIRSPEC slit by the fiber extraction unit (FEU). These fibers allow KPIC to spatially separate light from a planet from that of its host star. See Delorme et al. (2021) for an in-depth instrument summary.

[11] The literature defines κ And b variably, sometimes as a planetary-mass companion, bound companion, super-Jupiter, or low-mass brown dwarf (Carson et al. 2013; Hinkley et al. 2013; Stone et al. 2020; Uyama et al. 2020; Wilcomb et al. 2020). It is likely near or just below the limit for deuterium burning (Carson et al. 2013; Hinkley et al. 2013), but its orbital inclination may allow for disk formation by disk instability (Currie et al. 2018). We have chosen to refer to it as a planetary-mass companion or a planet.

2.2. Instrument Setup

When taking data, we direct light through KPIC into NIRSPEC. We use a custom pupil stop in NIRSPEC as the FEU creates a different optical beam than that of NIRSPEC when it is used directly behind the telescope or AO system. We use NIRSPEC's "Thin" filter, clear PK-50 glass that is used to suppress red leaks in JHK filters by blocking wavelengths longer than ~2.5 μm. Because the FEU pupil is different, we offset the PK-50 from it in nominal position to avoid vignetting from a central obscuration on the PK-50 substrate though since these observations, new K-band filter with better K-band transmission and no central obscuration have been installed in NIRSPEC. The NIRSPEC echelle grating was set to 63.°0, and the cross disperser was set to 35.°76, resulting in data containing nine spectra orders, NIRSPEC orders 31–39, ranging from approximately 1.94–2.49 μm. The disperser positions were held fixed for all of the data and calibrations described in this paper.

2.3. κ And b Observations

On UT 2020 July 3, we observed κ And b in K band using KPIC.

We began our observing sequence by designating a primary science fiber, based on which fiber had the best end-to-end throughput in daytime testing, as well as identifying which fiber was closest to the host star during our science observations, designating that fiber as our secondary. Using the adaptive optics field rotator (K-mirror), we rotated the field of view relative to our fixed fiber bundle such that this secondary fiber captured simultaneous stellar spectra while we observed the companion on the primary fiber but was not directly aligned closely enough to saturate on the host star during the longer exposure. These simultaneous stellar spectra were used in data exploration, but on-axis observations of the star were used for our final analysis.

We first placed the host star, κ And A, on the primary and secondary science fibers, taking three 30 s exposure in each position, for telluric calibration purposes. Using the FIU, we offset the star such that κ And b is placed on the primary science fiber, as shown in Figure 1. We then took 600 s exposures with NIRSPEC, capturing light from the companion, as well as scattered starlight, on the primary fiber, and significant starlight on the secondary fiber. Our remaining on-sky fibers also captured some starlight, as well as background. After our first hour of observations on the companion, we returned to the host star and repeated our calibration exposures before returning to the companion.

Our total integration time on κ And b was 100 minutes with ten 600 s exposures, over a range in air mass from 1.1 to 1.25.

2.4. Calibration Data

In addition to calibrating using the spectra of the host star obtained during the observing sequence, we derive our wavelength solution by observing an M-giant star. We observed M giant HIP 81497 (spectral type M2.5III), and telluric standard star Upsilon Herculis (spectral type B9III), which we observed twice during the night to check for wavelength solution shifts due to a M 4.6 earthquake near Maunakea during the night. Because all data on κ And b were taken afterwards, the calibration data after the quake were used for all further analyses though any shift was minimal. For these

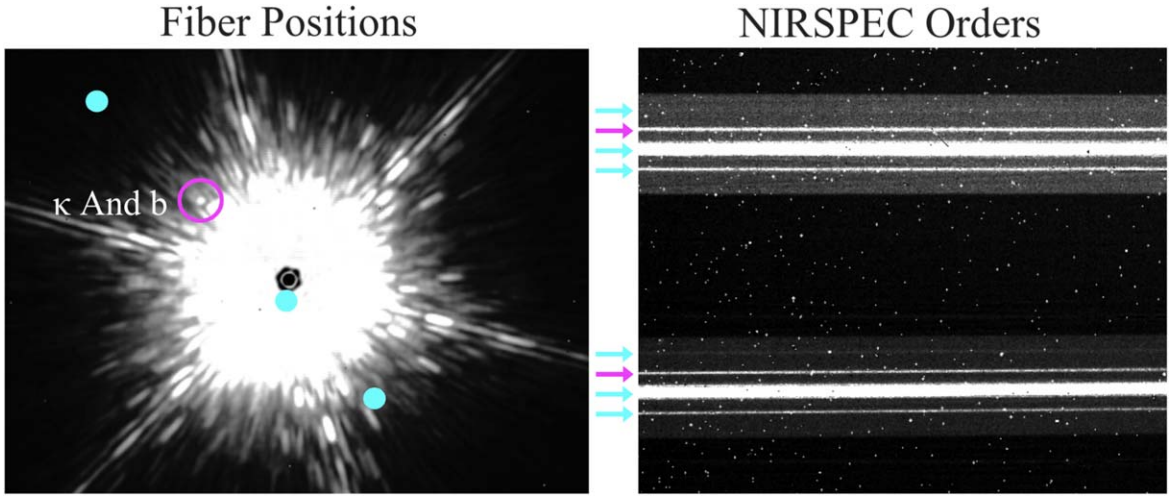

Figure 1. Visualization of the radial location of fibers, shown on sky and on the NIRSPEC detector when observing with the KPIC FIU. One fiber is placed on the companion, one fiber is placed near the star, and the other fibers capture varying amount of stellar light. This NIRC2 image was not taken during the observing sequence but serves as an example of the dynamic range of the stellar halo though a coronagraph is not used during KPIC observations, so there is a slight difference. The right-hand image is a small portion of two echelle orders on the NIRSPEC detector, showing a portion of the fiber traces in those orders.

calibrations, we took five 1.5 s exposures of HIP 81497 and three 30 s exposures of ups Her on axis in each of the four science fibers on slit that night. The dominant thermal noise in our data is from NIRSPEC, so after the end of the night, we took a series of thermal background frames at each exposure time we used (600 s for science images, 1.5 s and 30 s for calibration images), for use in background subtraction and in identifying bad pixels. These capture the thermal background of KPIC when no light is being injected into any of the fibers in order to measure thermal emission from KPIC (Wang et al. 2021).

3. Data Reduction

3.1. Raw Data Reduction and Extraction

We reduce our data and extract spectra using a custom-built pipeline for KPIC data.[12] Our data are produced by NIRSPEC, so they share size and format with other NIRSPEC data taken since its most recent upgrade (2048 by 2048 pixels, NIRSPEC's order layout; Martin et al. 2018), but KPIC's fiber-fed configuration allows and requires us to modify the reduction process accordingly to take advantage of the stable traces and line spread function of the single-mode fiber.

Using the thermal background frames with exposure times coordinated to that of our science and calibration data, we create combined background frames using the mean of each set. We find the noise in each pixel by taking the standard deviation of values across all frames and use these to locate bad pixels on the NIRSPEC detector.

We subtract the appropriate background frames from our science and calibration data and mask identified bad pixels. These do not perfectly subtract off the background in our data, as the FEU is at a different temperature during the day when our background frames are taken. This residual background is modeled in the extraction step.

Instead of rectifying and extracting each order, we use data on the telluric standard to locate each fiber on the detector, allowing us to extract 1D spectra directly. The single-mode fibers we use produce a point-spread function (PSF) on the detector that is approximately a 2D Gaussian. By measuring the position and standard deviation of the PSF at each vertical column of the detector, we are able to identify each trace, fitting a spline to smooth these measured positions.

Before extracting, we account for the residual background leftover after an imperfect background subtraction, likely due to internal temperature differences within the instrument between daytime backgrounds and nighttime observations. We offset from the measured fiber trace, using pixels at least 5 pixels away from the center of a fiber, to estimate the remaining background in each column. We subtract the median of these pixels from each pixel in the column.

We use the trace calibration derived from the telluric standard to extract the spectra of in every column of each fiber. We use optimal extraction (Horne 1986) to measure the flux using a 1D Gaussian profile as the PSF, with positions and standard deviations determined by the trace measurements taken on the standard star. We fit for the amplitude of the Gaussian and convert amplitude to total flux, weighing each pixel by the noise computed from the background frames and photon noise from the data itself. The flux in each column of the fiber is the total integrated flux of this 1D Gaussian, using the uncertainty of the optimal extraction as the uncertainty in the flux measurement (Horne 1986). We repeat this measurement across the full slit and for every order, resulting in 9 orders of extracted 1D spectra with 2048 channels per order. We also measure the instrumental spectral response of each science fiber.

3.2. Wavelength Calibration

To derive a wavelength solution, we use data on each fiber from a bright M-giant star, HIP 81497, and compare the observed spectra to models. We compute the expected radial velocity (RV) shift of the star using barycentric correction and the systemic RV. We use a PHOENIX-ACES-AGSS-COND-2011 stellar model spectrum with a temperature of 3600 K (Husser et al. 2013), an ATRAN (Lord 1992) telluric transmission model of the atmosphere, and the spectral response of instrument to build a model of the starlight, adjusted for continuum and background. For each order, we fit

[12] https://github.com/kpicteam/kpic_pipeline

Table 1
System Properties

Parameter	Measurement	Source
Age (Myr)	47^{+27}_{-40}	Jones et al. (2016)
Mass ($M_{\rm Jup}$)	13^{+13}_{-2}	Currie et al. (2018)
Host RV (km s^{-1})	$-12.7^{+0.8}_{-0.8}$	Gontcharov (2006)
Host Mass ($M_{\odot}$)	$2.768^{+0.1}_{-0.1}$	Jones et al. (2016)
Host Spectral Type	B9IVn	Garrison & Gray (1994)
$T_{\rm eff}$ (K)	1700^{+100}_{-100}	This work
log(g) (cgs dex)	$4.7^{+0.5}_{-0.5}$	This work
RV (km s^{-1})	$-17.35^{+0.05}_{-0.09}$	This work
$v \sin(i)$ (km s^{-1})	$38.42^{+0.05}_{-0.05}$	This work

for wavelength using a cubic spline function, first performing a grid search with three nodes for an initial fit and then running a nonlinear simplex optimizer (Nelder–Mead) to identify a best fit.

4. Fitting High-resolution Spectra

4.1. Forward Modeling κ And b Spectra

When fitting our spectra of κ And b, we create a forward model of our data using the following method, defined in Wang et al. (2021).

We directly compare our extracted spectra to a forward model containing all expected companion, stellar, telluric, and background contributions (Ruffio et al. 2019). We also compare results to a model in which we include no signature of a companion as a baseline.

In order to create this model, we need to understand what light ends up in our fiber and on our detector, with contributions from the star, planet, atmosphere, telescope, and instrument.

Data from a fiber placed on a planet can described as follows (Wang et al. 2021):

$$D_p(\lambda) = \alpha_p(\lambda)T(\lambda)P(\lambda) + \alpha_s(\lambda)T(\lambda)S(\lambda) + n(\lambda). \quad (1)$$

In this equation, D_p represents light extracted from the planet fiber. T is optical system transmission, including components from the atmosphere, telescope, and instrument. P is the flux from the planet, and S is the flux from the star, while α_p is the coupling efficiency of planet light and α_s is the coupling efficiency of stellar speckles into the fiber. n is the noise, where the thermal background of the instrument is dominant. All parameters are functions of wavelength.

We calculated the transmission of the optical system using on-axis observations of κ And A. We use this to find T. We do not expect significant overlap with stellar spectral lines in K band for this stellar type, minimizing errors due to an imperfect stellar spectrum. We divide the on-axis spectra of the star by the model of the star, using a PHOENIX spectrum at 11,600 K (Husser et al. 2013) and use this to determine the transmission of planet light.

The remaining coupling terms vary slowly as a function of wavelength. As wavelength changes, differential atmospheric refraction slowly changes the apparent position on sky of the companion. Stellar speckle coupling can be approximated across K band as a low-order polynomial (Gravity Collaboration et al. 2020). These slow shifts mean that continuum subtraction using a high-pass filter can remove the effect of these terms in the data.

Continuum subtraction also allows us to disregard the low spectral frequency changes of the instrument transmission that are introduced by changes in air mass.

We high-pass filter using a median filter on the spectrum, using a 200 pixel ($\sim$0.004 μm) box to compute and then subtract from the original.

After high-pass filtering, we are able to fit directly to our data. We further assume that, after high-pass filtering (denoted by H), effects shared across components are negligible, allowing us to break down our approximation further, instead filtering components individually:

$$\mathcal{H}[D_p] \approx \mathcal{H}[\alpha_p TP] + \mathcal{H}[\alpha_s TS] + \mathcal{H}[n]. \quad (2)$$

We utilize this method initially described in Wang et al. (2021) to complete our further analysis, both for molecular detection and characterization of atmospheric parameters, radial velocity, and spin.

4.2. Molecular Detection

In order to confirm detection of the companion and identify molecules in the atmosphere of κ And b, we used a modified cross-correlation method, estimating the maximum likelihood for both the companion and stellar flux as a function of a shift in radial velocity space, as described in Wang et al. (2021). For each companion RV, scaling factors for the planet and star are calculated using a linear least-square optimization technique. Our cross-correlation function (CCF) is composed of resulting values for the planet scaling parameter divided by its uncertainty at each companion RV (Ruffio et al. 2019). From our data, we use orders 31–33 (seen in Figure 2) for this analysis, consistent with the locations of molecular features for H_2O, CO, and CH_4.

We generate our planet models, based on the Sonora-Bobcat grid of temperature–pressure profiles (Marley et al. 2018, 2021), allowing us to generate single-molecule models for cross correlation. This is an equilibrium chemistry model without clouds, but we found the CCF signal of a combined CO+H_2O model to be consistent within 10% of the CCF signal-to-noise ratio (S/N), in comparison to BT-Settl models, which has clouds consistent with our expectations for this object, indicating that molecular detection is not dependent on cloud assumptions. We used model opacities from Freedman et al. (2008, 2014), utilizing the CH_4 line lists from Hargreaves et al. (2020) and H_2O line lists from Barber et al. (2006).

Using this method, we produced single-molecule models and models combining several molecules. For κ And b, we used a model with an effective temperature of 1800 K and a surface gravity of log(g) = 4.5. We found these detections to be relatively insensitive to choice of effective temperature and surface gravity.

We computed CCFs using CO, H_2O, and CH_4 molecular templates for the planet data. We computed the same CCF for extracted spectra that we expected to only contain noise, both from fibers that were not on the companion but observe similar stellar flux, and from offsetting our extraction to areas of the slit without a fiber, which are dominated by the thermal background. In our CCFs, we included velocity offsets between -500 and 500 km s^{-1} from the solar system barycenter. We normalized each CCF by dividing by the standard deviation of

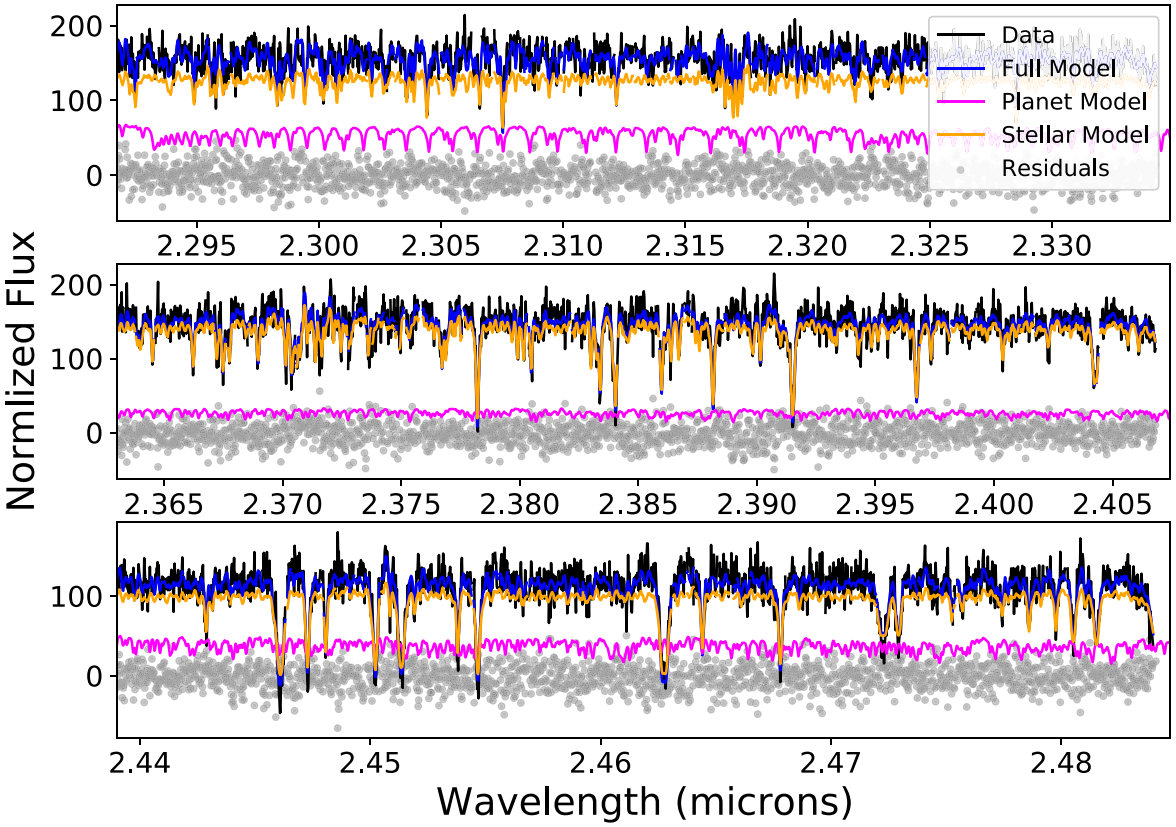

Figure 2. Extracted spectra in NIRSPEC orders 31–33 used in the fit compared to the best-fitting forward model for that order, with contributions from companion and speckle flux also shown independently.

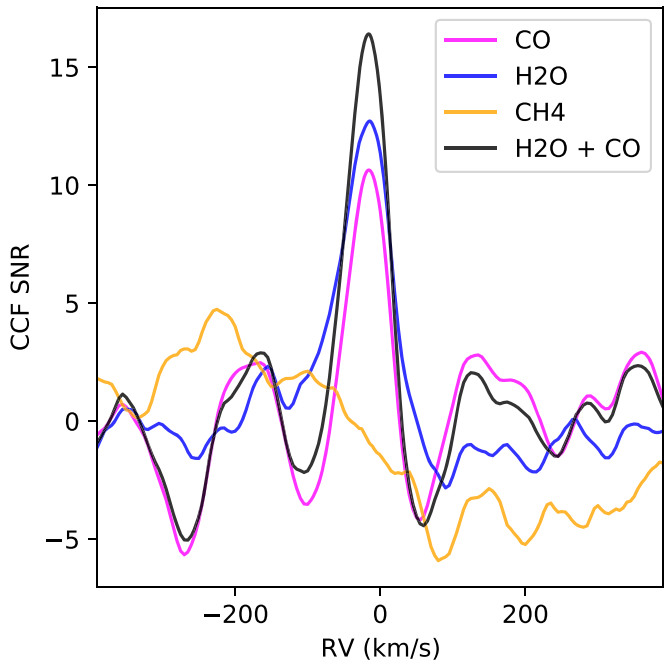

Figure 3. Cross correlations for individual molecular species. Detections of H_2O, CO, and expected nondetection of CH_4.

all noise spectral CCFs for that given molecule, giving us CCF S/N functions.

We find a strong detection of CO and H_2O in the atmosphere of κ And b and no detection of CH_4. Our CCF S/N for H_2O alone is 12.7, CO alone is 10.6, and the combined H_2O and CO model is 16.4. Our strongest detection of the planet using this method was using the model containing both CO and H_2O. Our nondetection of CH_4 is consistent with the effective temperature we measure, and the width of the CCF is consistent with fast rotation. The CCF S/N functions for each molecule are plotted in Figure 3.

4.3. Companion Spin, Radial Velocity, and Atmospheric Parameters

We used the same forward-modeling approach to fit for the rotational broadening ($v \sin(i)$) of κ And b's spectrum using the BT-Settl model grid, as well as confirm previously constrained atmospheric and bulk parameters for the companion and measure RV.

For this analysis, we simultaneously fit the companion's temperature, surface gravity, rotational broadening, and radial velocity relative to the solar system barycenter, as well as the planet flux and the stellar speckles at the planet location. We fit these parameters using a Markov Chain Monte Carlo (MCMC) method built on the emcee package, which is an implementation of the affine-invariant ensemble sampler (Goodman & Weare 2010; Foreman-Mackey et al. 2013). Our MCMC run used 100 walkers, 5000 steps, including a burn in of 2000 steps.

For the planet spectrum component (P) of our forward model, we fit the BT-Settl model grid to our data, varying effective temperature ($T_{\rm eff}$) and surface gravity ($\log(g)$ in centimeter gram second; Allard et al. 2012). We selected these models as BT-Settl is the only publicly available grid available at a high enough spectral resolution ($R > 35{,}000$) that includes clouds, present on all objects of this temperature, and

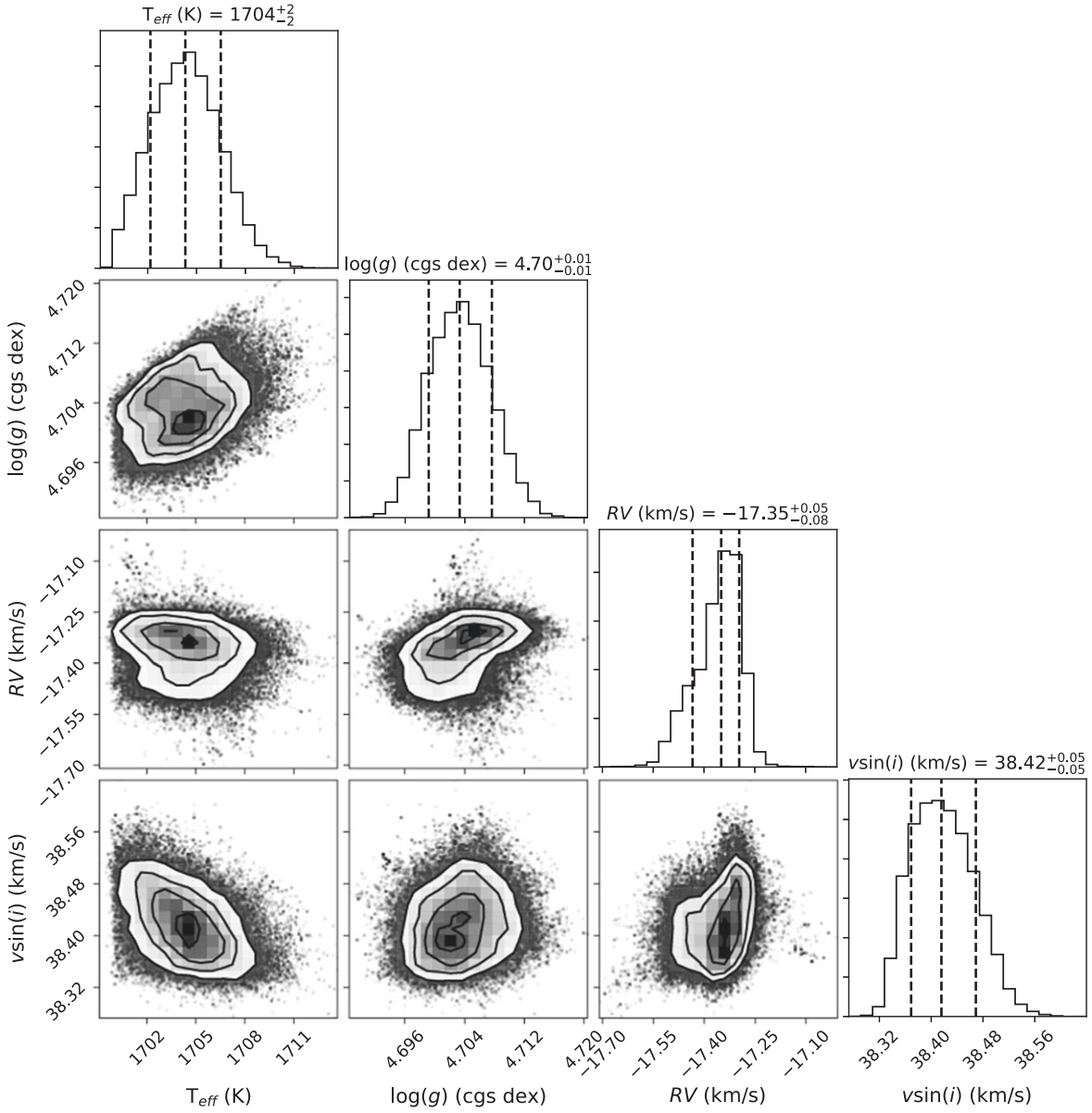

Figure 4. Corner plot corresponding to the MCMC fit to the BT-Settl model grid. Marginalized posteriors are shown on the diagonal, with covariance between all parameters in corresponding 2D histograms. Dashed lines show 16th, 50th, and 84th percentile statistical errors. Although this analysis results in small statistical error bars for temperature and log(g), this is not a realistic representation of our constraints on these terms. We instead adopt errors the size of the grid spacing for the rest of the paper as our analysis strongly prefers grid points. Measurements for spin and RV are insensitive to changes of temperature or log(g) as large as the grid spacing; see Section 5.1.

confirmed present for κ And b based on photometry and low resolution spectroscopy (Stone et al. 2020; Uyama et al. 2020). We limited by the spacing of the model grid, which offers steps of 100 K and we interpolate between, and take this as our error due to strong preference for the grid points themselves.

We fit for the planet RV relative to the solar system barycenter but note that the host star's radial velocity is not well known, so relative RV measurements are difficult but compare to existing values in the literature there as well.

The host star RV is not very well constrained because of its spectral type of B9IVn, with estimates of $-12.7 \pm 0.8\,\mathrm{km\,s^{-1}}$ (Gontcharov 2006) and $-11.87 \pm 1.53\,\mathrm{km\,s^{-1}}$ (Becker et al. 2015), and we use $-12.7 \pm 0.8\,\mathrm{km\,s^{-1}}$ due to the smaller uncertainty in the measurement.

We use the `fastRotBroad` function in `PyAstronomy` (Czesla et al. 2019) to fit the rotational broadening ($v \sin(i)$) of our companion spectrum.

Additionally, in preliminary analysis, we found higher-than-expected uncorrelated noise than that predicted by our formal optimal extraction errors when extracting the fluxes from the traces on the detector. We believe the noise to be caused by an underestimation of extraction errors or an unaccounted for noise term, to be explored in future analysis of instrumental noise and or data pipeline improvements. For the purpose of this work, we fit for this additional noise term in the MCMC, assuming it to be Gaussian. In this, the total error $\sigma^2_{\rm tot} = \sigma^2_{\rm pipe} + \sigma^2_{\rm fit}$, where $\sigma_{\rm pipe}$ is the nominal extraction error from our pipeline and $\sigma_{\rm fit}$ is the error term we fit for. We used a

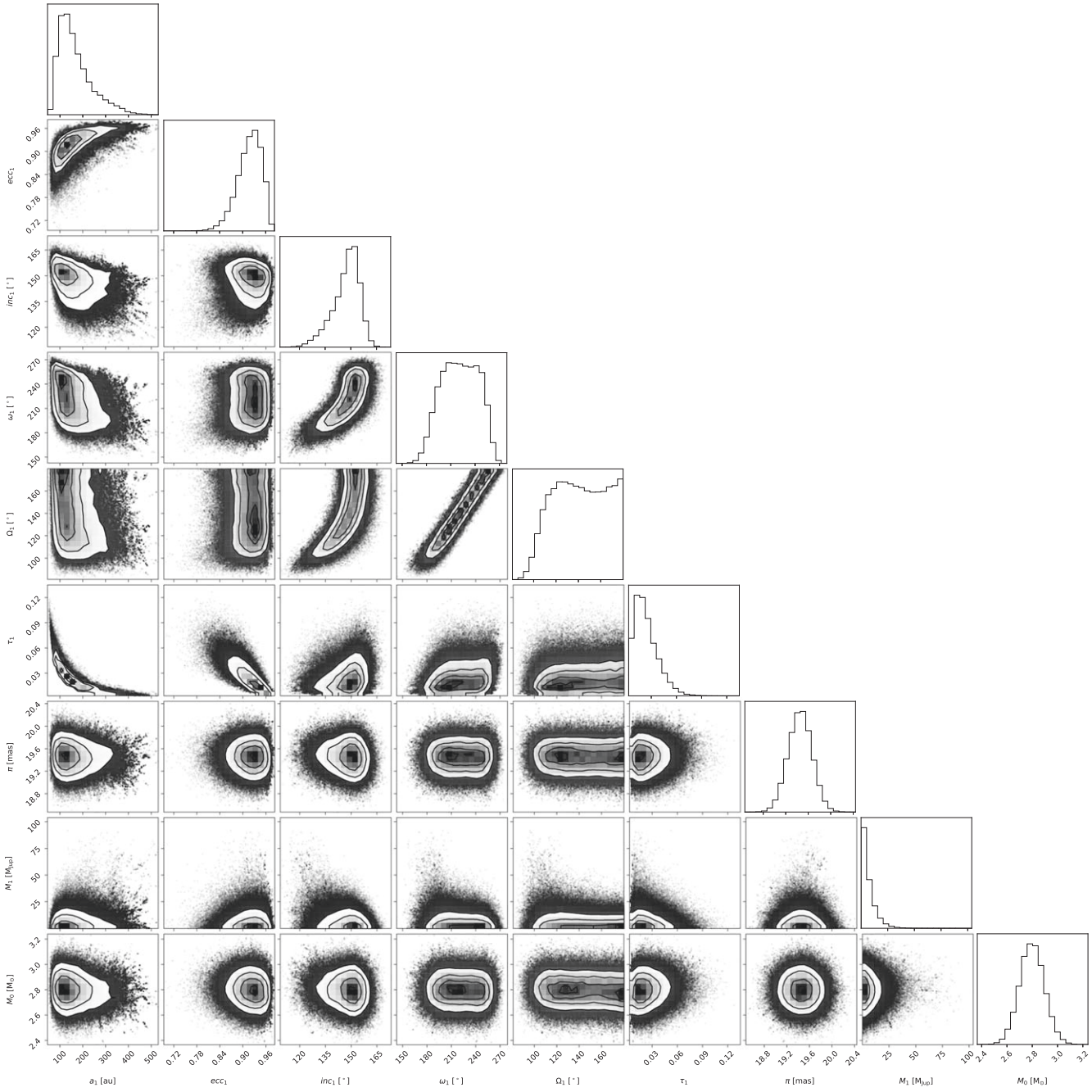

Figure 5. Posteriors of the best-fit orbital solutions for κ And b using companion RVs, astrometry (Bowler et al. 2020), and the HGCA (Brandt 2021) with the orbitize! package (Blunt et al. 2020).

Table 2
Orbit Posteriors

Parameter	Posterior
a (au)	$101.96^{+50.36}_{-27.37}$
e	$0.88^{+0.03}_{-0.04}$
i (deg)	$148.05^{+10.94}_{-14.59}$
π (mas)	$19.45^{+0.21}_{-0.21}$
ω (deg)	$200.85^{+30.81}_{-18.40}$
Ω (deg)	$115.85^{+32.01}_{-15.46}$
τ	$0.04^{+0.02}_{-0.02}$
M_1 ($M_{\rm Jup}$)	$4.61^{+7.58}_{-3.44}$
M_0 ($M_\odot$)	$2.79^{+0.10}_{-0.10}$

separate $\sigma_{\rm fit}$ for each spectral order but assumed that $\sigma_{\rm fit}$ is constant in each order. This approximation appears suitable based on analysis of fit residuals.

Our log likelihood as described in Wang et al. (2021) is defined as

$$\ln(\mathcal{L}) = -\frac{1}{2}\sum\left(\frac{(\mathcal{H}[D_p] - \mathcal{H}[M_p])^2}{\sigma_{\rm tot}^2} + \ln(2\pi\sigma_{\rm tot}^2)\right). \quad (3)$$

Here, we sum over each spectral channel in our data. M_p includes planet and stellar speckle parameters.

For each free parameter, we assumed a uniform prior. Effective temperature ($T_{\rm eff}$) was assumed to be between 1000

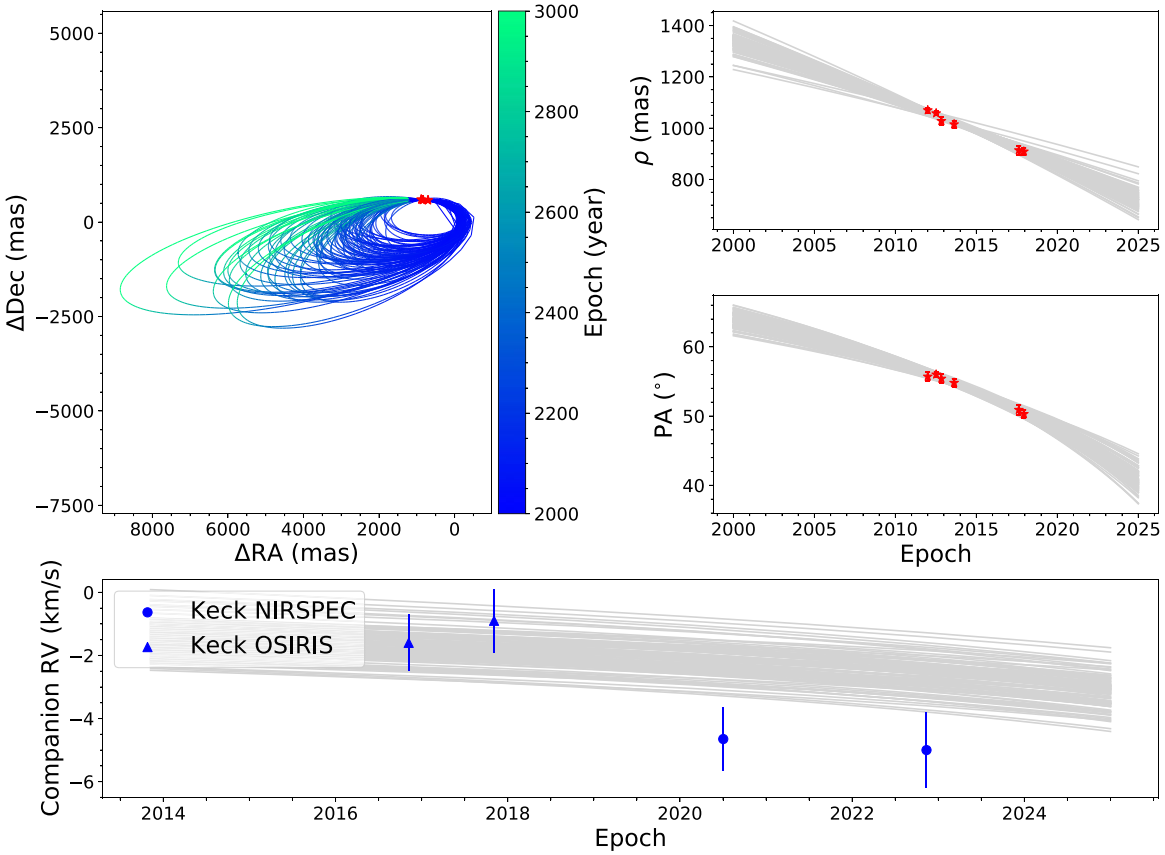

Figure 6. Best-fit 100 random draw orbits for κ And b, using companion RVs and the HGCA (Brandt 2021) with the orbitize! package. Upper left: ΔR.A. and Δdecl. coordinate best fits for the κ And b system (blue/green lines) and the relative astrometry (red stars) from Bowler et al. (2020). Upper right, top: separation (ρ) in milliarcsecond best fits (gray lines) with relative astrometry (red stars) from Bowler et al. (2020); Upper right, bottom: position angles (PAs) in degree best fits (gray lines) with the relative astrometry (red stars) from Bowler et al. (2020). Middle: RV orbit best fits (gray lines) for the host star κ And A. Bottom: RV orbit best fits (gray lines) for the κ And b using KPIC measurements (blue triangles).

and 2200 K, surface gravity ($\log(g)$) between 3.5 and 5.5, companion radial velocity −150 and 150 km s^{-1}, rotational broadening ($v \sin(i)$) between 0 and 80 km s^{-1}, planet flux 0–100 DN (data numbers; also called analog digital unit or ADU), stellar speckles flux from 0 to 500 DN for each order, and our additional noise term ($\sigma_{\rm fit}$) from 0 to 100 DN for each order.

Results of our MCMC fits for temperature, $\log(g)$, radial velocity, and $v \sin(i)$ are shown in Figure 4 and in Table 1. We assessed the model fit by plotting the best-fitting parameters to each order of our data used in the fit, seen in Figure 2. On visual inspection, our forward models appear to fit the data. Residuals of the fit appear to be dominated by uncorrelated noise, which we confirm by computing the autocorrelation function (ACF) of the residuals. The ACF is well approximated by a delta function, with the wings of the ACF having an amplitude of $\leqslant$5% of the peak, suggesting that an uncorrelated noise model is sufficient, likely dominated by thermal noise in the instrument.

5. Discussion

5.1. Atmospheric Parameters

We detect CO and H_2O but not CH_4 in our analysis of high-resolution spectra of κ And b. This finding is consistent with previous studies of the object at lower resolution (Stone et al. 2020; Wilcomb et al. 2020). We detected each molecule independently but found the highest correlation to a combined model.

We obtain a fit on bulk atmospheric properties from our forward-model fits to the data. We find that our results are consistent with previous work. However, these findings are highly model dependent. Our effective temperature measurement of 1700^{+100}_{-100} K is consistent with lower-resolution analysis, but prior work measures a range of temperatures as low as 1600 K and as high as 2200 K (Stone et al. 2020; Uyama et al. 2020; Wilcomb et al. 2020). The systematic error of our fits is higher than the statistical error. Previous studies do not consistently constrain $\log(g)$, but many find it in the range of 4.0–4.5. We find the same model dependence, with a best fit of $4.7^{+0.5}_{-0.5}$, higher than would be consistent with prior results. Discrepancies among results for $\log(g)$ are expected, as high-resolution spectroscopy is not as reliable for $\log(g)$ measurements. Wang et al. (2021) also found higher $\log(g)$ for the HR 8799 planets than in the literature from lower-resolution observations. We use the BT-Settl models, which use equilibrium chemistry, where there could be disequilibrium chemistry effects, depending on temperature. However, other publicly available models with clouds are not available at a high enough resolution, so we were not able to use these to compare.

We did not observe a strong correlation between values for radial velocity and planetary spin and our measured bulk

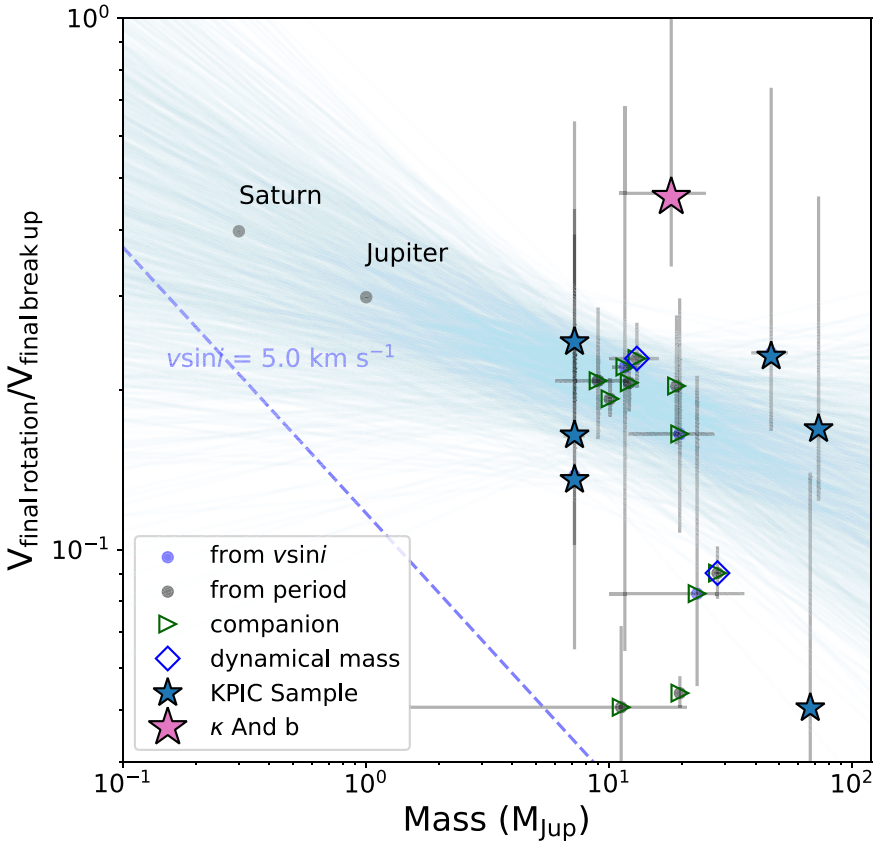

Figure 7. Spin measurements from low-mass companions and solar system planets, with those from the published KPIC sample marked with a star. κ And b, shown with a pink star, is one of the highest points in this comparison. Other known companions are marked with a green triangle, and known dynamical mass measurements are marked with a blue diamond. Detection limits for $v \sin(i)$ ($\leqslant 5$ km s^{-1}) are indicated by blue dashed line. We also include random draws from the Wang et al. (2021) solutions for the best-fit rotational trend, in light blue.

atmospheric parameters, mitigating the propagation of issues with our atmospheric measurements into the rest of our analysis, but these inconsistencies could nevertheless bias our measurements. We fit with broad atmospheric priors to address this issue and identify a consistent radial velocity in our single-molecule fits, which are instead derived from the Sonora model grid. We also tested fixed values for $T_{\rm eff}$ and $\log(g)$, finding no measurable shift in radial velocity and spin.

5.2. Orbital Fit

We perform an orbit fit using existing astrometry data, compiled in Bowler et al. (2020), with the addition of our KPIC radial velocity points. We include the radial velocity point from this study, which we measure to be $-17.35^{+0.05}_{-0.09}$ km s^{-1}, as well as another KPIC point on this object from Xuan (2024) of $-17.7^{+0.9}_{-0.9}$ km s^{-1}, and compare to points from Wilcomb et al. (2020). We used the orbitize! package to run an MCMC to jointly fit our radial velocity and astrometry data on the system (Blunt et al. 2020), using the Hipparcos-Gaia (Early Data Release 3) Catalog of Accelerations (HGCA; Brandt 2021). We used a parallax value of 19.4064 ± 0.2104 mas (Gaia Collaboration et al. 2021) and a stellar mass value of $2.768 \pm 0.1\,M_{\odot}$ (Jones et al. 2016). We set a prior on companion mass of 0.0–0.1 $M_{\odot}$. Our orbitize! MCMC run used 1000 walkers; 50,000 steps; and 20 walker temperatures to improve avoidance of local minima. Results of this run are shown in Figure 5, and posteriors are listed in Table 2.

We find our RV measurements to fall lower than expectations for the orbit but within our uncertainty range, as seen in Figure 6. Our relative RV is also affected by the significant uncertainty in the stellar radial velocity itself. Our RV addition does not significantly change or constrain the understood orbit of κ And b. We compared to fits found in the literature and also ran the same orbit fit excluding RV points. In comparing to Wilcomb et al. (2020), we find that most of our overlapping parameters (i, ω, Ω) fit within the 1σ range defined there.

5.3. Spin Analysis

We measured the spin of κ And b for the first time via analysis of the $v \sin(i)$ of $38.42^{+0.05}_{-0.05}$ km s^{-1} and compared this to a population of companions with measured spins. We compared to the population assessed in Bryan et al. (2020), as well as other early results from KPIC, including Wang et al. (2021) and Hsu (2024). We excluded tenuous measurements. We included the rotation periods of Saturn and Jupiter in our analysis.

We use the method described in Wang et al. (2021) and Hsu (2024) to convert our $v \sin(i)$ measurement to a final rotational velocity v in order to compare it to the predicted breakup velocity of κ And b in Figure 7. In that analysis, spins are parameterized as rotational velocity over breakup velocity. Assuming uniform inclination distributions, the geometric sine distribution is used to convert $v \sin(i)$ into a rotational velocity, and inferred age, mass, and radii are used to compute the breakup velocity. In order to minimize differences based on age

in the analysis, these rotation points are evolved to 5 Gyr assuming conservation of angular momentum as the final rotation velocity and the final breakup velocity (Wang et al. 2021; Hsu, 2024).

We see that our measurement falls within expectations for the population though significantly on the higher end of this range, rotating at a speed much closer to the breakup velocity than most objects in the sample. The measured $V_{\rm final\ rotation}/V_{\rm final\ break\ up}$ for κ And b is $0.461^{+0.797}_{-0.127}$, with a $V_{\rm final\ rotation}$ of $85.1^{+144.8}_{-23.9}$ km s^{-1} and a $V_{\rm final\ break\ up}$ of $184.9^{+28.3}_{-22.8}$ km s^{-1}. This rotation measurement is close to 50% of breakup velocity, where most objects in the sample are closer to 10%.

We add our data point to the analysis begun in Wang et al. (2021) and continued in Hsu (2024). In this, we focused our analysis on companions that are likely to share a planet-like formation history. We did not focus on spin measurements for free-floating brown dwarfs, which may have formed through different mechanisms. However, Bryan et al. (2020) argue for a single-spin regulation mechanism, independent of formation scenario.

Additional data points allow us to improve constraints on the relationship between mass and spin in this regime, as well as investigate how spin evolves for these objects, though a strong evaluation of this relationship is not yet possible. To date, there are both few overall spin measurements, but also only a small subset of these are bound, directly imaged companions close to their host star.

This area of parameter space is opened up significantly by KPIC, with its ability to push closer to the star. These initial measurements for κ And b add important information in the higher-spin velocity regime, as this object's rotation speed is one of the highest relative to breakup measured to date.

We measure κ And b to have a $v\sin(i)$ of $38.42^{+0.05}_{-0.05}$ km s^{-1} and put this measurement in context with the currently measured population in order to investigate a spin–mass relationship.

6. Conclusion

We obtained high-resolution K-band spectra of κ And b taken by KPIC. We used cross-correlation methods to detect CO and H_2O at high significance in the planetary atmosphere, with CCF S/Ns of 10.6 and 12.7 respectively and 16.4 combined, and registered a nondetection of CH_4. We used a forward-modeling, likelihood-based framework to fit atmospheric parameters, radial velocity, and spin of the planet while simultaneously fitting for the stellar speckles present in the data.

For effective temperature, we measure 1700^{+100}_{-100} K, which is limited by our model grid size. This value is consistent with some prior lower-resolution findings though these have varied widely between 1600 and 2200 K (Stone et al. 2020; Uyama et al. 2020; Wilcomb et al. 2020). For $\log(g)$, we measure $4.7^{+0.5}_{-0.5}$ cgs dex, higher than expected based on previous studies. We identify a radial velocity for κ And b of $-17.35^{+0.05}_{-0.09}$ km s^{-1}, which is consistent with another KPIC data point from a separate analysis, $-17.7^{+0.9}_{-0.9}$ km s^{-1} (Xuan 2024), and falls slightly below our best orbit fit. We measured the spin of κ And b for the first time at $38.42^{+0.05}_{-0.05}$ km s^{-1}, finding it to be high in comparison to the rest of the currently measured population of bound companions, closer to 50% of breakup velocity, rather than the 10% that is closer to standard for existing rotational measurements of bound companions.

6.1. Future Prospects

For κ And b, further investigation would help particularly for studies of the planet's radial velocity. Improved information on the κ And A would significantly improve existing and future RV points, as our error in relative RV is dominated by the error in stellar RV. More precise RV data on the planet would also improve our orbit fit.

We would also benefit from high-resolution analysis of the planet at other wavelengths. Searching a wider range of wavelengths and comparing to models with an updated line list for CH_4 and other molecules could yield detections not possible in this study though this is not necessarily expected within the κ And b temperature range.

Our spin-trend analysis would benefit from a wider population of studied bound companions, particularly those in the planetary-mass regime. This is possible with KPIC, and some studies are already underway to widen this sample (Hsu 2024; Xuan 2024). Future upgrades to KPIC, as well as other existing and planned instruments (current: Very Large Telescope (VLT)/CRIRES+; Follert et al. 2014; VLT/HiRISE, Otten et al. 2021; Subaru/REACH, Kotani et al. 2020; future: Keck/HISPEC, Thirty Meter Telescope/MODHIS; Mawet et al. 2022; Konopacky et al. 2023; Extremely Large Telescope/ANDES; Marconi et al. 2022) will both expand on the sample of studied bound and low-mass companions. Hardware improvements will enable greater sensitivity and higher precision, leading to better rotation, radial velocity, and atmospheric measurements.

Acknowledgments

Funding for KPIC has been provided by the California Institute of Technology, the Jet Propulsion Laboratory, the Heising-Simons Foundation (grant No. 2015-129, No. 2017-318, No. 2019-1312, No. 2023-4598), the Simons Foundation (through the Caltech Center for Comparative Planetary Evolution), and the NSF under grant AST-1611623. J.X. is supported by the NASA Future Investigators in NASA Earth and Space Science and Technology (FINESST) award No. 80NSSC23K1434.

Data presented in this work were obtained at the W. M. Keck Observatory, which is operated as a scientific partnership among the California Institute of Technology, the University of California and the National Aeronautics and Space Administration. The Observatory was made possible by the generous financial support of the W. M. Keck Foundation. We wish to recognize and acknowledge the very significant cultural role and reverence that the summit of Maunakea has always had within the indigenous Hawaiian community. We are most fortunate to have the opportunity to conduct observations from this mountain.

Facility: Keck:II (KPIC).

Software: `astropy` (Astropy Collaboration et al. 2018), `scipy` (Virtanen et al. 2020), `PyAstronomy` (Czesla et al. 2019), `emcee` (Foreman-Mackey et al. 2013), `corner` (Foreman-Mackey 2016), `orbitize!` (Blunt et al. 2020).

ORCID iDs

Evan C. Morris https://orcid.org/0000-0003-3165-0922
Jason J. Wang (王劲飞) https://orcid.org/0000-0003-0774-6502
Chih-Chun Hsu https://orcid.org/0000-0002-5370-7494

Jean-Baptiste Ruffio https://orcid.org/0000-0003-2233-4821
Jerry W. Xuan https://orcid.org/0000-0002-6618-1137
Jacques-Robert Delorme https://orcid.org/0000-0001-8953-1008
Callie Hood https://orcid.org/0000-0003-1150-7889
Marta L. Bryan https://orcid.org/0000-0002-6076-5967
Emily C. Martin https://orcid.org/0000-0002-0618-5128
Dimitri Mawet https://orcid.org/0000-0002-8895-4735
Andrew Skemer https://orcid.org/0000-0001-6098-3924
Ashley Baker https://orcid.org/0000-0002-6525-7013
Benjamin Calvin https://orcid.org/0000-0003-4737-5486
Daniel Echeverri https://orcid.org/0000-0002-1583-2040
Luke Finnerty https://orcid.org/0000-0002-1392-0768
Michael P. Fitzgerald https://orcid.org/0000-0002-0176-8973
Nemanja Jovanovic https://orcid.org/0000-0001-5213-6207
Joshua Liberman https://orcid.org/0000-0002-4934-3042
Ronald Lopez https://orcid.org/0000-0002-2019-4995
Ben Sappey https://orcid.org/0000-0003-1399-3593
J. Kent Wallace https://orcid.org/0000-0001-5299-6899
Ji Wang (王吉) https://orcid.org/0000-0002-4361-8885

References

Allard, F., Homeier, D., & Freytag, B. 2012, RSPTA, 370, 2765
Astropy Collaboration, Price-Whelan, A. M., Sipőcz, B. M., et al. 2018, AJ, 156, 123
Barber, R. J., Tennyson, J., Harris, G. J., & Tolchenov, R. N. 2006, MNRAS, 368, 1087
Batygin, K. 2018, AJ, 155, 178
Becker, J. C., Johnson, J. A., Vanderburg, A., & Morton, T. D. 2015, ApJS, 217, 29
Bell, C. P. M., Mamajek, E. E., & Naylor, T. 2015, MNRAS, 454, 593
Blunt, S., Wang, J. J., Angelo, I., et al. 2020, AJ, 159, 89
Bowler, B. P., Blunt, S. C., & Nielsen, E. L. 2020, AJ, 159, 63
Brandt, T. D. 2021, ApJS, 254, 42
Brogi, M., & Line, M. R. 2019, AJ, 157, 114
Bryan, M. L., Ginzburg, S., Chiang, E., et al. 2020, ApJ, 905, 37
Carson, J., Thalmann, C., Janson, M., et al. 2013, ApJL, 763, L32
Currie, T., Brandt, T. D., Uyama, T., et al. 2018, AJ, 156, 291
Czesla, S., Schröter, S., Schneider, C. P., et al., 2019 PyA: Python Astronomy-related Packages, Astrophysics Source Code Library, ascl:1906.010
Delorme, J.-R., Jovanovic, N., Echeverri, D., et al. 2021, JATIS, 7, 035006
Follert, R., Dorn, R. J., Oliva, E., et al. 2014, Proc. SPIE, 9147, 914719
Foreman-Mackey, D. 2016, JOSS, 1, 24
Foreman-Mackey, D., Hogg, D. W., Lang, D., & Goodman, J. 2013, PASP, 125, 306
Freedman, R. S., Lustig-Yaeger, J., Fortney, J. J., et al. 2014, ApJS, 214, 25
Freedman, R. S., Marley, M. S., & Lodders, K. 2008, ApJS, 174, 504
Gaia Collaboration, Brown, A. G. A., Vallenari, A., et al. 2021, A&A, 650, C3
Garrison, R. F., & Gray, R. O. 1994, AJ, 107, 1556
Gontcharov, G. A. 2006, A&AT, 25, 145
Goodman, J., & Weare, J. 2010, CAMCOS, 5, 65
Gravity Collaboration, Nowak, M., Lacour, S., et al. 2020, A&A, 633, A110
Hargreaves, R. J., Gordon, I. E., Rey, M., et al. 2020, ApJS, 247, 55
Hinkley, S., Pueyo, L., Faherty, J. K., et al. 2013, ApJ, 779, 153
Horne, K. 1986, PASP, 98, 609
Hsu, C.-C., Wang, J. J., Xuan, J. W., et al. 2024, ApJ, 971, 9
Husser, T. O., Wende-von Berg, S., Dreizler, S., et al. 2013, A&A, 553, A6
Jones, J., White, R. J., Quinn, S., et al. 2016, ApJL, 822, L3
Jovanovic, N., Delorme, J.-R., Bond, C. Z., et al. 2019, Proc. SPIE, 11117, 111170T
Konopacky, Q. M., Baker, A. D., Mawet, D., et al. 2023, Proc. SPIE, 12680, 1268007
Konopacky, Q. M., Barman, T. S., Macintosh, B. A., & Marois, C. 2013, Sci, 339, 1398
Kotani, T., Kawahara, H., Ishizuka, M., et al. 2020, Proc. SPIE, 11448, 1144878
Landman, R., Stolker, T., Snellen, I., et al. 2024, A&A, 682, A48
Lord, S. D. 1992, Technical Memorandum 103957, NASA
Marconi, A., Abreu, M., Adibekyan, V., et al. 2022, Proc. SPIE, 12184, 1218424
Marley, M., Saumon, D., Morley, C., & Fortney, J. 2018, Sonora 2018: Cloud-free, Solar Composition, Solar C/O Substellar Atmosphere Models and Spectra, nc_m+0.0_co1.0_v1.0, Zenodo, doi:10.5281/zenodo.1309035
Marley, M. S., Saumon, D., Visscher, C., et al. 2021, ApJ, 920, 85
Martin, E. C., Fitzgerald, M. P., McLean, I. S., et al. 2018, Proc. SPIE, 10702, 107020A
Mawet, D., Delorme, J. R., Jovanovic, N., et al. 2017, Proc. SPIE, 10400, 1040029
Mawet, D., Fitzgerald, M. P., Konopacky, Q., et al. 2022, Proc. SPIE, 12184, 121841R
McLean, I. S., Becklin, E. E., Bendiksen, O., et al. 1998, Proc. SPIE, 3354, 566
Otten, G. P. P. L., Vigan, A., Muslimov, E., et al. 2021, A&A, 646, A150
Ruffio, J.-B., Macintosh, B., Konopacky, Q. M., et al. 2019, AJ, 158, 200
Snellen, I. A. G., Brandl, B. R., de Kok, R. J., et al. 2014, Natur, 509, 63
Stone, J. M., Barman, T., Skemer, A. J., et al. 2020, AJ, 160, 262
Uyama, T., Currie, T., Hori, Y., et al. 2020, AJ, 159, 40
Virtanen, P., Gommers, R., Oliphant, T. E., et al. 2020, NatMe, 17, 261
Wang, J., Kolecki, J. R., Ruffio, J.-B., et al. 2022, AJ, 163, 189
Wang, J. J., Ruffio, J.-B., Morris, E., et al. 2021, AJ, 162, 148
Wang, J., Wang, J. J., Ruffio, J.-B., et al. 2023, AJ, 165, 4
Wilcomb, K. K., Konopacky, Q. M., Barman, T. S., et al. 2020, AJ, 160, 207
Xuan, J. W., Hsu, C.-C., Finnerty, L., et al. 2024, ApJ, 970, 40
Xuan, J. W., Wang, J., Finnerty, L., et al. 2024, ApJ, 962, 10
Xuan, J. W., Wang, J., Ruffio, J.-B., et al. 2022, ApJ, 937, 54
Zuckerman, B., Rhee, J. H., Song, I., & Bessell, M. S. 2011, ApJ, 732, 61